optica

Blind sparse inpainting reveals cytoskeletal filaments with sub-Nyquist localization: supplementary material

YANHUA WANG,[1,2] SHU JIA,[3] HAO ZHANG,[4] DOORY KIM,[5,6] HAZEN BABCOCK,[5,6] XIAOWEI ZHUANG,[5,6,7] AND LESLIE YING[1,*]

[1]Department of Biomedical Engineering, Department of Electrical Engineering, University at Buffalo, the State University of New York, Buffalo, New York, USA
[2]School of Information and Electronics, Beijing Institute of Technology, Beijing, China
[3]Department of Biomedical Engineering, Stony Brook University, the State University of New York, Stony Brook, New York, USA
[4]Department of Biomedical Engineering, Northwestern University, Evanston, Illinois, USA
[5]Department of Chemistry and Chemical Biology, Harvard University, Cambridge, Massachusetts, USA
[6]Howard Hughes Medical Institute, Harvard University, Cambridge, Massachusetts, USA
[7]Department of Physics, Harvard University, Cambridge, Massachusetts, USA
*Corresponding author: leiying@buffalo.edu

Published 12 October 2017

This document provides supplementary information to "Blind sparse inpainting reveals cytoskeletal filaments with sub-Nyquist localization," https://doi.org/10.1364/OPTICA.4.001277. Details about the algorithm and further simulation and experimental results are included.

https://doi.org/10.6084/m9.figshare.5421508

1. THE CURVELET TRANSFORM

The curvelet transform is a powerful nonadaptive multiresolution geometric analysis technique that provides a directional multiscale decomposition of images [S1]. At each scale, the curvelet functions (or curvelets) are generated from a 'mother' curvelet by translations and rotations. As a consequence, the curvelet functions $\varphi_{j,k,l}(\mathbf{r})$ ($\mathbf{r}\in\mathbb{R}^2$) have three parameters: j is the scale index, k implies the location in the spatial domain, and l indicates the orientation. The 'mother' curvelet $\varphi_j(\mathbf{r})$ at scale 2^j ($j\in\mathbb{N}_0$) is formulated as the spatial counterpart of a polar 'wedge' shaped window function in the frequency domain. The rotation operation is then performed by multiplying the coordinates $\mathbf{r}$ by a rotation matrix $\mathbf{R}_{\theta_{j,l}}$ with the following form:

$$\mathbf{R}_{\theta_{j,l}} = \begin{bmatrix} \cos\theta_{j,l} & \sin\theta_{j,l} \\ -\sin\theta_{j,l} & \cos\theta_{j,l} \end{bmatrix}, \tag{S1}$$

where $\theta_{j,l} = 2\pi\cdot 2^{-\lfloor j/2\rfloor}\cdot l$, $\lfloor j/2\rfloor$ extracts the integer part of $j/2$, and $0\le l\le 2^{\lfloor j/2\rfloor}-1$. Finally, the location parameter k represents a translation to the position of $\mathbf{p}_k^{(j,l)} = \mathbf{R}_{\theta_{j,l}}^{-1}\cdot[k_1\cdot 2^{-j}, k_2\cdot 2^{j/2}]^T$ ($k_1, k_2\in\mathbb{Z}$).

Based on the above parameters, $\varphi_{j,k,l}(\mathbf{r})$ is defined by:

$$\varphi_{j,k,l}(\mathbf{r}) = \varphi_j\left(\mathbf{R}_{\theta_{j,l}}\left(\mathbf{r}-\mathbf{p}_k^{(j,l)}\right)\right). \tag{S2}$$

The curvelet coefficients of a given function $f(\mathbf{r})$ are simply computed by its inner product with the curvelets $\varphi_{j,k,l}$:

$$c_{j,k,l} = c(j,k,l) = \left\langle f(\mathbf{r}), \varphi_{j,k,l}(\mathbf{r})\right\rangle. \tag{S3}$$

The curvelet family is redundant, thus the curvelet transform is not orthogonal. However, the curvelets form a tight frame, which means that $f(\mathbf{r})$ can be exactly reconstructed from its curvelet coefficients:

$$\begin{aligned} f(\mathbf{r}) &= \sum_{j,k,l} c_{j,k,l}\varphi_{j,k,l}(\mathbf{r}) \\ &= \sum_{j,k,l}\left\langle f(\mathbf{r}), \varphi_{j,k,l}(\mathbf{r})\right\rangle \varphi_{j,k,l}(\mathbf{r}) \end{aligned}. \tag{S4}$$

Figure S1 shows an example of curvelet. It is noted that the 'mother' curvelets have a parabolic scaling property. The effective length and width of $\varphi_j(\mathbf{r})$ ($j > 0$) obey the anisotropy scaling relation: width $\approx$ length^2. Furthermore, a curvelet is highly

direction sensitive due to the rotation operation. These two characteristics enable curvelet transform to provide sparse representations for images with linear and curvilinear features.

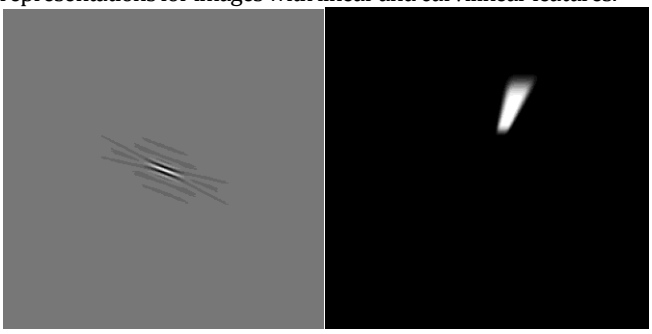

Fig. S1. An example of a curvelet (left) and its Fourier transform (right)

In this paper, we use CurveLab[S2] as the implementation of the discrete curvelet transforms (DCT). It has two implementations: curvelets via unequally spaced fast Fourier transform (USFFT) and curvelets via wrapping. The latter approach is simpler to understand and implement and it is of lower computational complexity as well. Therefore, we adopt curvelets via wrapping in the paper and abbreviate it by DCTW. Roughly speaking, DCTW consists of four steps: 2D FFT, windowing, frequency wrapping, and 2D inverse FFT.

The discrete curvelet transform of $\mathbf{x}$ can be expressed as:

$$\mathbf{c} = \mathbf{\Phi x}\,, \tag{S5}$$

where $\mathbf{\Phi} \in \mathbb{R}^{K\times N}$ ($K>N$) is composed of the conjugates of discretized curvelets obtained by DCTW. The inverse transform is then:

$$\hat{\mathbf{x}} = \mathbf{\Phi}^H \mathbf{c}\,. \tag{S6}$$

where H denotes the conjugate transpose of a matrix. The tight frame property ensures that $\mathbf{\Phi}^H\mathbf{\Phi} = \mathbf{I}$ and $\hat{\mathbf{x}} = \mathbf{x}$. However, it should be noted that $\mathbf{\Phi}\mathbf{\Phi}^H \neq \mathbf{I}$ in general.

2. RECONSTRUCTION STEPS

Figure S2 shows the complete flowchart of our blind sparse inpainting method for fast SMLM. The image acquisition setups are the same as conventional SMLM (or existing fast SMLM) expect that the number of acquired frames is far below the routine requirement. The input is thus a sequence of raw diffraction-limited camera images and the output is a reconstructed Nyquist-density image. Detailed descriptions of the steps are as follows:

Step 1: Localization of molecules.

After the raw camera images are acquired, the first step is to estimate the positions of the emitting fluorescent molecules with an accuracy below the diffraction limit. This can be accomplished by any existing methods. The underlying results is a list containing the coordinates and intensity of each localization. Note that dense activation and its accompanying algorithm also can be employed to provide a faster imaging speed.

Step 2: Formulation of low-density image.

A 2D pixel grid is established to discretize the coordinate system. The spacing is in general set to one-half of the desired spatial resolution. The minimum number of grid must ensure the spatial size of the whole grid covers all the localization results. Then, each fluorophore is assigned to its nearest grid. If several fluorophores are projected onto a same grid, the sum of their intensities are used as the value of that grid. Since the number of frames used is relatively small, only a low density image is obtained after the projection of all fluorophores.

Step 3: preprocessing of low-density image.

Threshholding is an optional operation to account for the background noises or remove small valued disturbance. The threshold is either a predefined value or a statistic drawn from the histogram. Normalization of the image intensity is required so that λ can be set to the same value for different images once it is manually tuned. Such a fixed λ has shown to be robust for different images and can also reduce the workload.

Step 4: estimation of $\mathbf{P}_Q$.

The unique characteristics of SMLM images make it challenging to estimate $\mathbf{P}_Q$. Unlike natural images, the background is 'dark'. Therefore, the zero-valued pixels in the low density image can be either the background (corresponding elements of $\mathbf{P}_Q$ should be 1) or the foreground with fluorophores but not activated or detected (corresponding elements of $\mathbf{P}_Q$ should be 0). Also, the foreground texture is not that clear and smooth as well.

We adopt a simple approach from a straightforward intuition. We divide the non-zero part of $\mathbf{P}_Q$ into foreground part and background part. The foreground part is simply determined by the non-zero pixels on the enhanced low-density image. To determine whether a zero-valued pixel belongs to the background, we search its neighborhood to see if there exist a non-zero pixel. If all pixels in the neighborhood are zero, we believe it is in the background with a high probability and set the corresponding elements of $\mathbf{P}_Q$ to be 1.

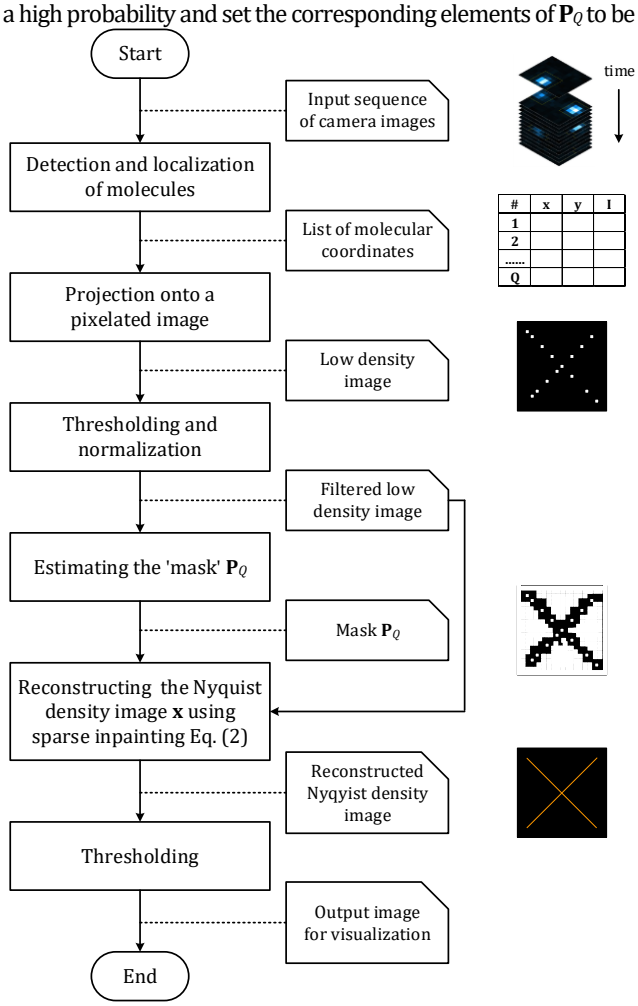

Fig. S2. Flowchart of blind sparse inpainting

Step 5: reconstruction of Nyquist density image.

The reconstruction is obtained by solving the L1 minimization problem in Equation (2). The optimization algorithm is detailed in the next section.

Step 6: thresholding of Nyquist density image.

To enhance the visualization effect and eliminate small valued artifacts, threshholding is sometimes a necessary step and we adopt a predefined threshold in this paper.

3. OPTIMIZATION ALGORITHM

The objective function is as follows:

$$\min_{\mathbf{x}} \ \|\mathbf{\Phi x}\|_1 + \frac{\lambda}{2} \ \|\mathbf{P}_Q\mathbf{x} - \mathbf{x}_Q\|_2^2 . \qquad \textbf{(S7)}$$

This is a classical L1 minimization problem and can be solved by various methods, such as linear programming and interior point method. Recently, variable splitting and augmented Lagrangian method (ALM) have proven to be efficient approaches to solve the L1 minimization problems. In general, these algorithms introduce auxiliary variables to decouple the sparsity terms with other parts. ALM is then applied to solve the modified constrained problem. In this paper, we focus on a specific variation of ALM called alternating direction method with multiplier (ADMM) [S3].

Introducing auxiliary variables $\mathbf{d} = \mathbf{\Phi x}$, we have the equivalent form of Equation (S7):

$$\min_{\mathbf{x}} \ \|\mathbf{d}\|_1 + \frac{\lambda}{2}\|\mathbf{P}_Q\mathbf{x} - \mathbf{x}_Q\|_2^2 \ \text{ s.t. } \mathbf{\Phi x} = \mathbf{d} . \qquad \textbf{(S8)}$$

The scaled form augmented Lagrangian function is:

$$L_\rho(\mathbf{d},\mathbf{x},\mathbf{u}) = \|\mathbf{d}\|_1 + \frac{\lambda}{2}\|\mathbf{P}_Q\mathbf{x} - \mathbf{x}_Q\|_2^2 + \frac{\rho}{2}\|\mathbf{\Phi x} - \mathbf{d} + \mathbf{u}\|_2^2 , \qquad \textbf{(S9)}$$

where $\mathbf{u}$ is the scaled dual variables. Based on ADMM, we derive the following iteration scheme:

$$\mathbf{x}^{k+1} = \arg\min_{\mathbf{x}} \ \frac{\lambda}{2}\|\mathbf{P}_Q\mathbf{x} - \mathbf{x}_Q\|_2^2 + \frac{\rho}{2}\|\mathbf{\Phi x} - \mathbf{d}^k + \mathbf{u}^k\|_2^2 , \qquad \textbf{(S10)}$$

$$\mathbf{d}^{k+1} = \arg\min_{\mathbf{d}} \ \|\mathbf{d}\|_1 + \frac{\rho}{2}\|\mathbf{\Phi x}^{k+1} - \mathbf{d} + \mathbf{u}^k\|_2^2 , \qquad \textbf{(S11)}$$

$$\mathbf{u}^{k+1} = \mathbf{u}^k + \mathbf{\Phi x}^{k+1} - \mathbf{d}^{k+1} . \qquad \textbf{(S12)}$$

The $\mathbf{x}$-subproblem has a closed form solution:

$$\mathbf{x}^{k+1} = \mathbf{B}(\lambda\mathbf{P}_Q^T\mathbf{x}_Q + \rho\mathbf{\Phi}^H(\mathbf{d}^k - \mathbf{u}^k)), \qquad \textbf{(S13)}$$

where $\mathbf{B} = (\lambda\mathbf{P}_Q^T\mathbf{P}_Q + \rho_1\mathbf{I})^{-1}$. The tight frame property of $\mathbf{\Phi}$ is used in the derivation. Since $\mathbf{P}_Q$ is diagonal, $\mathbf{B}$ can be easily calculated by diagonal element inversions.

The optimal value in $\mathbf{d}$-subproblem is obtained through the element-wise shrinkage operator:

$$d_i^{k+1} = \text{shrink}([\mathbf{\Phi x}^{k+1}]_i + u_i^k, \ 1/\rho_1) , \qquad \textbf{(S14)}$$

where $\text{shrink}(x,\gamma) = \text{sgn}(x)\cdot\max(x - \gamma, 0)$.

4. ERROR BOUNDS

Given the blind nature of the proposed method (that is $\mathbf{P}_Q$ is unknown), theoretical analysis of error bounds is challenging. Here we assume the location of the acquired region $\mathbf{P}_Q$ is known, and the performance of sparsity-based inpainting can be analyzed using asymptotic analysis as in Reference [S4].

Suppose that $\mathbf{x}$ lies in a Hilbert space $\mathcal{H}$ which can be decomposed into a direct sum

$$\mathrm{H} = \mathrm{H}_M \oplus \mathrm{H}_K , \qquad \textbf{(S15)}$$

where subspace $\mathcal{H}_M$ is associated with the missing part of $\mathbf{x}$ and subspace $\mathcal{H}_K$ relates to the known part of $\mathbf{x}$.

Define the concentration on $\mathcal{H}_M$ as

$$\kappa = \kappa(\Lambda, \mathrm{H}_M) = \sup_{f \in \mathrm{H}_M} \frac{\|\mathbf{1}_\Lambda \mathbf{\Phi f}\|_1}{\|\mathbf{\Phi f}\|_1} , \qquad \textbf{(S16)}$$

where $\mathbf{1}_\Lambda$ is the indicator function that takes the value 1 on Λ and 0 on Λ^c, with Λ being an index set of coefficients and Λ^c is the complementary set.

Define $\mathbf{x}$ is δ-clustered sparse in $\mathbf{\Phi}$ with respect to Λ if

$$\|\mathbf{1}_\Lambda \mathbf{\Phi f}\|_1 \le \delta , \qquad \textbf{(S17)}$$

then in noise-free case, the reconstruction error is bounded by

$$\|\hat{\mathbf{x}} - \mathbf{x}\|_2 \le \frac{2\delta}{1 - 2\kappa} , \qquad \textbf{(S18)}$$

and in noisy case such that $\|\mathbf{\Phi n}\|_1 \le \varepsilon$ where $\mathbf{n}$ is the noise vector, the reconstruction error is bounded by

$$\|\hat{\mathbf{x}} - \mathbf{x}\|_2 \le \frac{2\delta + (3 + 2\kappa)\varepsilon}{1 - 2\kappa} . \qquad \textbf{(S19)}$$

Note that both the concentration and the clustered sparsity depend on the chosen set of indices Λ. The explicit knowledge of Λ is not necessary because it is only an analysis tool. In practice, the correct choice of Λ is a key problem. In our sparse inpainting optimization scheme, this is automatic performed in solving the d-subproblem (i.e. Equation (S11)) by soft-thresholding, which is shown to be able to provide a good estimation [S4].

5. SUPPLEMENTARY SIMULATION RESULTS

A. Reconstruction for different numbers of frames

Figure S3 shows blind sparse inpainting reconstructions for different numbers of frames at 40nm nominal resolution. The result from 400 frames is very close to the Nyquist-density image in Figure 1. Even in the 150 frame case, the reconstruction can still visually reveal the structures.

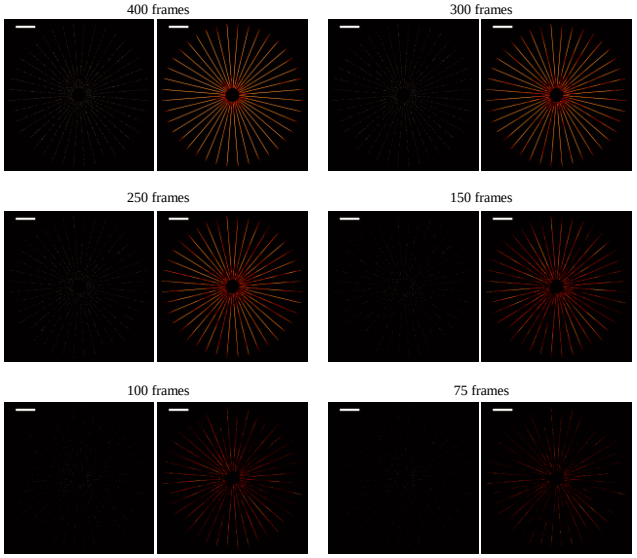

Fig. S3. Simulation results of low-density image (left) and blind sparse inpainting reconstruction (right) for different numbers of frames at 40nm nominal resolution. Scale bars: 2μm.

B. Reconstruction for different resolutions

Figure S4 shows blind sparse inpainting reconstruction at nominal resolutions from 40nm to 120nm. The numbers of frames is determined to ensure the true positive rate in the reconstruction is above 95%. In this case, the Nyquist resolution is approximately the same as the nominal resolution. When the resolution is poorer than 80nm, the inner ends of the radial bars are too close to be resolved.

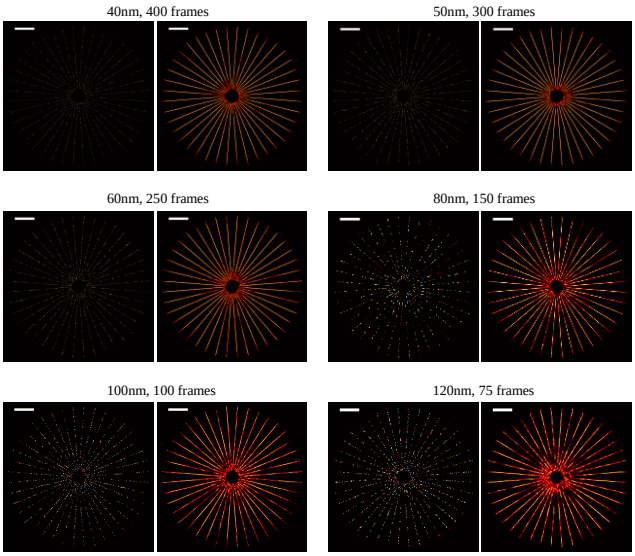

Fig. S4. Simulation results of low-density image (left) and blind sparse inpainting reconstruction (right) at nominal resolutions from 40nm to 120nm. Scale bars: 2μm.

6. SUPPLEMENTARY MICROTUBULE RESULTS

Figure S5 shows the results on the third real microtubule dataset. Blind inpainting from 400 frames can preserve the spatial resolution as well as the high-density image from 32000 frames.

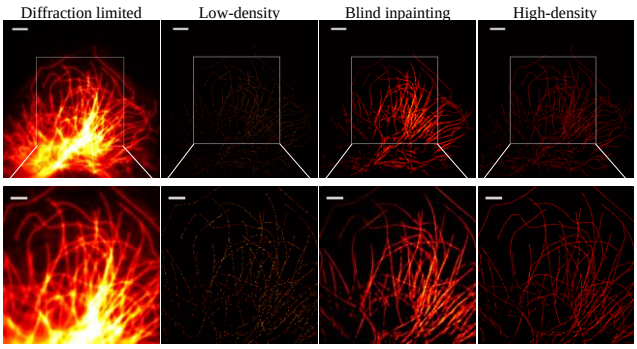

Fig. S5. Results on the third real microtubule dataset (top: full field of view with scale bars of 4μm, bottom: ROI with scale bars of 2.5μm). Pixel size: 53nm.

7. SUPPLEMENTARY ACTIN RESULTS

Figure S6 shows real actin STORM data. The blind sparse inpainting was applied on the low-density image synthesized from 1000 frames, and the result is seen to be close to the Nyquist-density image synthesized from all 115000 frames. The white squares indicate the ROIs, with one shown in Figure 8 of the main text.

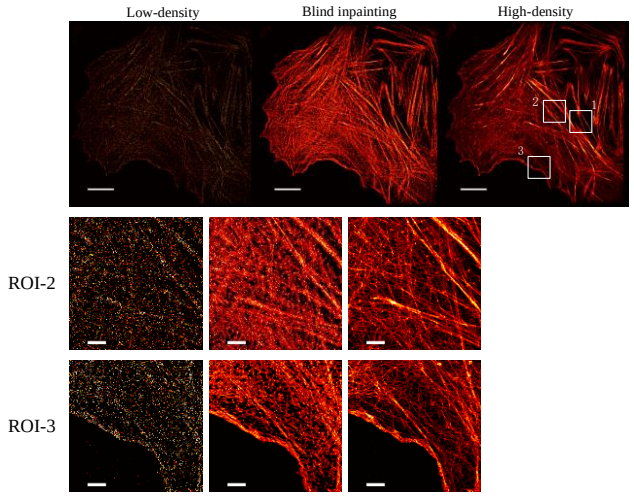

Fig. S6. Results on real actin STORM data. Scale bars: 4μm in full images and 1.25μm in ROI images, pixel size: 35nm.

References

1. E. Candès, L. Demanet, D. Donoho, and L. Ying, "Fast discrete curvelet transforms," Multiscale Model. Simul. **5**, 861-899 (2006).
2. http://www.curvelet.org/
3. S. Boyd, N. Parikh, E. Chu, B. Peleato, and J. Eckstein, "Distributed optimization and statistical learning via the alternating direction method of multipliers," Foundation and Trends in Machine Learning **3**, 1-122 (2011).
4. E. J. King, G. Kutynlok, and X. Zhuang, "Analysis of inpainting via clustered sparsity and microlocal Analysis," J. Math. Imaging Vis. **48**, 205-234 (2014).